Photon avalanche effect in $LaCl_3:Pr^{3+}$

Delena Bell Gatch, W. M. Dennis, and William M. Yen
Department of Physics and Astronomy, University of Georgia, Athens, Georgia 30602-2451
(Received 3 May 2000)

The phenomenon of photon avalanche, which involves both an excited state absorption process from a metastable level and a cross relaxation energy transfer process responsible for the large increases in population of this metastable level, has been investigated in $LaCl_3:Pr^{3+}$. In this paper, we report on the intensity dependence of both the steady-state fluorescence and the temporal evolution of the avalanche signal as a function of temperature (80 K to room temperature). Comparisons are made between experimental results and mathematical models based on a six-level system described by a series of coupled rate equations combined with the propagation of a Gaussian beam. We develop a model with only one adjustable parameter, the excited state absorption cross section, which provides a good description of all of our experimental data. We have estimated values of the excited state absorption cross section for the various $^3H_5 \rightarrow {}^3P_0$ pumping transitions at different temperatures.

I. INTRODUCTION

The phenomenon of photon avalanche was first reported in 1979 by Chivian, Case, and Eden.[1] It was an unexpected discovery resulting from an investigation of the infrared quantum-counter process[2] in $LaCl_3$ and $LaBr_3$ crystals doped with Pr^{3+}. In their infrared-visible double resonance experiment, the infrared pump beam was used to excite from the ground state ($^3H_4$) to the first excited state ($^3H_5$), while the visible pump beam was resonant with the $^3H_5 \rightarrow {}^3P_1$ excited state transition. When their visible pump radiation was slightly greater than a certain critical intensity, the fluorescence from the ^3P_J levels was observed to increase by several orders of magnitude. Correspondingly, the absorption at the visible pump frequency was sufficient to cause a dimming of the laser beam as it propagated through the crystal. They attributed this phenomenon to an efficient cross relaxation energy transfer between neighboring Pr^{3+} ions, $(^3H_6, {}^3H_4) \rightarrow (^3H_5, {}^3H_5)$, which left both ions with population in the $^3H_5$ manifold thereby enhancing the excited state absorption (ESA) used in the quantum-counter process. They also observed that the IR pump source was not necessary for this process which they denoted photon avalanche. The mechanism responsible for the initial population of the $^3H_5$ manifold was not considered at this time. Later it was proposed[3] that the $^3H_5$ level was populated by off–resonance pumping from the ground state followed by relaxation to the $^3H_5$ manifold.

Photon avalanche is an unconventional continuous wave (cw) pumping mechanism that leads to strong upconverted emission without resonant ground state absorption (GSA). The essential conditions needed for the observation of photon avalanche include: (1) the existence of an intermediate metastable storage level which acts as a reservoir for the pump energy, (2) optical pumping between this storage level and some higher lying state, and (3) a cross relaxation process which sustains the population of the storage level. The photon avalanche phenomenon usually occurs in a system which has a high ratio of ESA to GSA at the pump frequency. In general, the input laser frequency should be resonant with a transition between the storage level and a higher lying state. The relaxation from this higher lying state must then lead to a cross relaxation process that results in a nonlinear buildup of population in the storage level. The relaxation rates from states above which the cross relaxation process originates must have higher probabilities than the relaxation rates to the levels below which the cross relaxation process originates. The cross relaxation process must also have a higher probability than radiative or nonradiative (multiphonon) relaxation to lower levels.

Several distinctive aspects of the photon avalanche phenomenon have been identified in the literature.[3,4] The main feature of the avalanche process is the existence of a critical threshold for the input laser intensity, which separates the output fluorescence into two regimes. Below threshold, an excited state population cannot be sustained and fluorescence is either weak or unobservable. Above threshold, a nonlinear increase in fluorescence occurs with an increase in pump intensity. This threshold behavior can be understood, in terms of the competing relaxation processes mentioned above. Another distinctive feature of avalanche is that the absorbency of the crystal depends upon the input laser intensity. Below threshold, the crystal is transparent to the pump beam; whereas, above threshold, the pump beam is strongly absorbed by the crystal. Last, the buildup of the avalanche fluorescence is also strongly dependent on the pump intensity. At threshold, there is a qualitative change in the shape of the transient signal as well as a slowing of the buildup time. A review of these and other aspects of the photon avalanche phenomenon is given by Joubert and references therein.[5]

The primary purpose of this paper is to construct a detailed model of photon avalanche in $LaCl_3:Pr^{3+}$ and to compare this model to experimental results. Section II is devoted to the discussion of experimental details. Section III describes the rate equation model used for analysis, and the numerical results are discussed in Sec. IV. The six-level system of coupled rate equations combined with the propagation of a Gaussian beam is shown to provide a good quantitative description of the observed behavior. Conclusions are given in Sec. V.

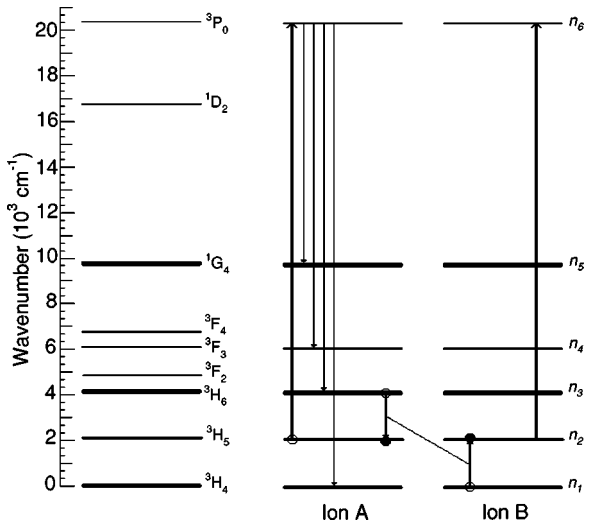

FIG. 1. Energy level diagram of Pr^{3+} and schematic diagram of the photon avalanche phenomenon. The excited state pump transition, dominant fluorescence transitions out of $^3P_0$, and cross relaxation process between neighboring ions are indicated by arrows.

II. EXPERIMENTAL PROCEDURES AND RESULTS

The photon avalanche mechanism for our experiments is represented schematically in Fig. 1 along with a partial $4f$ energy level diagram for Pr^{3+} in $LaCl_3$. In our experiments, a cw tunable dye laser is resonant with one of the $^3H_5 \rightarrow {}^3P_0$ excited state transitions. Since $LaCl_3$ is a soft material with a maximum phonon energy of only 210 cm^{-1}, nonradiative relaxation processes become very inefficient for energy gaps larger than several hundred wave numbers. Thus, the $^3H_5$ manifold, with a lifetime of 42 ms, is able to serve as the storage reservoir for the pump energy. Once the $^3P_0$ level has been populated via ESA, most of its population is funneled through the $^3H_6$ manifold during the radiative relaxation process. Due to the high Pr^{3+} concentration, population in the $^3H_6$ manifold may then relax by a $(^3H_6, {}^3H_4) \rightarrow (^3H_5, {}^3H_5)$ cross relaxation process with a nearby Pr^{3+} ion in the ground state. As a result of this cross relaxation process, two Pr^{3+} ions with population in the $^3H_5$ manifold are available for subsequent absorption of the pump beam resulting in further nonlinear build up of the $^3H_5$ population and hence dramatic increases in the $^3P_0$ fluorescence.

A crystal of $LaCl_3$ doped with Pr^{3+} at a concentration of 8 at% was used in these experiments. The crystal was grown from a melt using the Bridgman technique. Starting materials for the growth process consisted of $LaCl_3$ and $PrCl_3$ powders melted in an atmosphere of HCl (10%) and He (90%). The melt, contained in a 10-mm-diam fused silica tube, was crystallized by pulling at a rate of 2.5 mm/h through a temperature gradient of 25 °C/cm. After growth, the crystal was cut and polished to a size of approximately 5 mm$\times$3 mm$\times$1 mm such that the crystal c axis was parallel to the longest side. The crystal was then mounted in a variable temperature cryostat, which enabled us to perform measurements at temperatures between 80 K and room temperature using liquid nitrogen. Laser excitation was achieved using a Coherent Radiation model 699 ring dye laser pumped by a cw Spectra Physics argon ion laser. The wavelength of the dye laser could be tuned from 528 to 560 nm using a 2 $\times 10^{-3}$ M solution of pyrromethene 556 dye dissolved in ethylene glycol. The use of intracavity etalons prevented mode hopping as well as narrowed the linewidth of the laser to $\approx$20 MHz. Dove prisms were used to rotate the polarization of the pump beam, and a shutter was used to gate the cw laser beam so that the buildup of the fluorescence could be monitored. The pump beam was focused onto the broad surface of the crystal with a 150 mm focal length lens. The measured radius of the beam waist was 40 μm ($1/e^2$ irradiance). The emission from the ^3P_J levels was collected using a fiber optic bundle at 90° to the input laser beam direction. An OG–590 cutoff filter was placed before the fiber in order to block scattered laser light. Having the fiber bundle split into two portions, enabled the collection of two types of data simultaneously. Steady-state emission spectra were recorded with an EG&G Instruments 1530-A/AUV 1024S charge-coupled device detector in the spectral region of 640 nm. Time dependent measurements of the emission from $^3P_0 \rightarrow {}^3F_2$ were recorded by monitoring the output of an Oriel 77341 photomultiplier tube with a Tektronix TDS 460A digital oscilloscope. The emission was spectrally filtered using a monocrometer. Data consisted of sets of steady-state emission spectra and transient signals where the pump beam was varied from 5 to 300 mW using neutral density filters. It was important that both of these data sets be taken simultaneously, in order to eliminate small long term drifts which would prevent a direct comparison of the results. The power incident on the focusing lens was measured using a Newport 2835-C power meter, of which 88% was transmitted into the sample.

On pumping from the $^3H_5$ manifold to the $^3P_0$ level, we identified two transitions that resulted in photon avalanche. The first transition occurs under σ-polarized excitation at 546.1 nm, in close agreement with the expected position of the $^3H_5(II) \rightarrow {}^3P_0$ transition. The second transition occurs under π-polarized excitation at 547.2 nm, in close agreement with the expected position of the $^3H_5(IV) \rightarrow {}^3P_0$ transition. In studying the temperature dependence of these two transitions, we found that as the sample was heated to room temperature, the output fluorescence from the $^3P_0$ level reduced while the critical thresholds remained the same for both transitions. The buildup time required to reach the steady-state avalanche signal became shorter near threshold as the temperature was increased. The 546.1 nm transition exhibits stronger fluorescence, lower thresholds, and shorter buildup times than the 547.2 nm transition for each of the temperatures investigated. The 546.1 nm transition has a critical intensity threshold of approximately 600 W/cm^2; whereas, the 547.2 nm transition has a threshold intensity of approximately 2000 W/cm^2. These thresholds are much larger than those presented by Chivian, Case, and Eden[1] who report a range of critical pump intensities of 1.2–12.2 W/cm^2 for transitions around 530 and 546 nm.

III. RATE EQUATIONS

To our knowledge, the manner in which we include the initial population of the $^3H_5$ level and the inclusion of multiple interionic energy transfer processes in our rate equation analysis differs from those modeling schemes previously reported in the literature.

TABLE I. All of the interionic processes considered in our model exhibit direct spectral overlap between donor emission and acceptor absorption. Shown are the emission process, its bandwidth ΔE_{em}, the absorption process that leads to direct overlap of emission and absorption, and its bandwidth ΔE_{abs}.

Cross relaxation	Emission	$\Delta E_{em}(\mathrm{cm}^{-1})$	Absorption	$\Delta E_{abs}(\mathrm{cm}^{-1})$
x_a	$^3F_3 \rightarrow {}^3H_5$	3998-4236	$^3H_4 \rightarrow {}^3H_6$	4039-4382
x_b	$^3F_3 \rightarrow {}^3H_6$	1902-2132	$^3H_5 \rightarrow {}^3H_6$	1953-2248
x_c	$^3F_3 \rightarrow {}^3H_6$	1902-2132	$^3H_4 \rightarrow {}^3H_5$	1935-2286
x_d	$^3H_6 \rightarrow {}^3H_5$	1953-2248	$^3H_4 \rightarrow {}^3H_5$	1935-2286

The $^3H_5 \rightarrow {}^3P_0$ transition in $LaCl_3:Pr^{3+}$ can be resonantly pumped at a wavelength that is not resonant with a ground state transition. In our experiments the excited state transition $^3H_5 \rightarrow {}^3P_0$ was pumped. On average this requires an input energy of around 18 291 cm^{-1}. This same amount of energy applied toward a ground state transition would place an electron 1697 cm^{-1} above the $^1D_2$ manifold. Since the pump wavelength does not correspond to a resonant electronic absorption from the ground state, this pumping scheme seems unlikely. Usually the first step of the photon avalanche phenomenon is treated as an anti-Stokes multiphonon absorption.[6] Typically those modeling avalanche systems have included as their starting mechanism a nonresonant ground state pumping term proportional to the excited state pumping term. It is in this way that our modeling differs from those previously presented in the literature. We rely entirely on the initial thermal population of the $^3H_5$ manifold for providing the initial population necessary for achieving ESA. In our attempt to model our data by including an off-resonance GSA pumping term in our rate equations, we found the ratio of the GSA to the ESA R_{GSA}/R_{ESA} became so small that the thermal distribution between the lower two levels became the dominant mechanism for placing population in the $^3H_5$ manifold. For example, at room temperature (300 K) a value of less than 5×10^{-5} was necessary for R_{GSA}/R_{ESA} in order to fit the power dependent steady-state emission data. For smaller values, the model including off-resonance ground state pumping became identical to the model which relied only on the thermal population distribution between the lower two levels. In trying to find an acceptable fit for our low temperature data (100 K) an even smaller value for R_{GSA}/R_{ESA} was determined to be necessary. Other values reported for R_{GSA}/R_{ESA} are given here as a comparison. Lenth and MacFarlane reported a value of 1×10^{-4} for $YLiF_4:Nd^{3+}$;[7] Joubert, Guy, and Jacquier gave a value of 1.7×10^{-4} for the same material at 6 K.[8] Auzel and Chen report a value of 5×10^{-6} for $LiYF_4:Er^{3+}$ at room temperature.[9] Collings and Silversmith published a value of 2.0×10^{-3} for $LaF_3:Tm^{3+}$ at 77 K.[10] Guy, Joubert, and Jacquier determined a value of 5×10^{-4} for $YAG:Tm^{3+}$ at 33 K.[11] The values for R_{GSA}/R_{ESA} are expected to vary depending on the material being investigated, but the values we report are generally smaller than those given in the literature.

Several interionic energy transfer processes are known to occur in $LaCl_3:Pr^{3+}$. We have identified four cross relaxation processes and their associated upconversion processes that play an important role in photon avalanche in this system. All of these processes exhibit direct spectral overlap between donor emission and acceptor absorption, as can be seen in Table I. Our inclusion of all interionic energy transfer processes which have direct spectral overlap is different from the modeling of most avalanche systems discussed in the literature. Usually only those cross relaxation processes that feed directly into the storage level are included. Using this approach we were unable to obtain good agreement between our experimental results and our rate equation model. When including only the $(^3H_6,{}^3H_4)\rightarrow({}^3H_5,{}^3H_5)$ cross relaxation process, which is the only cross relaxation process that leaves two ions in the intermediate metastable level, a larger increase in fluorescence was predicted than observed experimentally. Recently, Wermuth and Güdel reported the necessity of including multiple cross relaxation and upconversion processes, specifically those involving excited state transitions, when modeling photon avalanche.[12] They found that the inclusion of these energy transfer processes were critical in describing the system under high power excitation where the population density of the excited states becomes significant.

The $^3F_2$ and $^3F_4$ levels rapidly thermalize with the $^3H_6$ and $^3F_3$ levels, respectively, effectively coupling these levels.[13] In the text, we will indicate thermally coupled sets of states by $\{\}$.

We have determined that photon avalanche in $LaCl_3:Pr^{3+}$ can adequately be described by the following six rate equations where n_1, n_2, n_3, n_4, n_5, and n_6 denote the populations in $^3H_4$, $^3H_5$, $\{^3F_2,{}^3H_6\}$, $\{^3F_4,{}^3F_3\}$, $^1G_4$, and $^3P_0$ respectively:

$$\dot{n}_1 = -\tau_{th}^{-1}n_1 + b_{61}\tau_6^{-1}n_6 + b_{51}\tau_5^{-1}n_5 + b_{41}\tau_4^{-1}n_4 + b_{31}\tau_3^{-1}n_3 + \tau_2^{-1}n_2 - x_a n_4 n_1 + \upsilon_a n_3 n_2 - x_c n_4 n_1 + \upsilon_c n_3 n_2 - x_d n_3 n_1 + \upsilon_d n_2^2, \quad (1)$$

$$\dot{n}_2 = -R_{26}n_2 + \tau_{th}^{-1}n_1 + b_{52}\tau_5^{-1}n_5 + b_{42}\tau_4^{-1}n_4 + b_{32}\tau_3^{-1}n_3 - \tau_2^{-1}n_2 + x_a n_4 n_1 - \upsilon_a n_3 n_2 - x_b n_4 n_2 + \upsilon_b n_3^2 + x_c n_4 n_1 - \upsilon_c n_3 n_2 + 2x_d n_3 n_1 - 2\upsilon_d n_2^2, \quad (2)$$

$$\dot{n}_3 = b_{63}\tau_6^{-1}n_6 + b_{53}\tau_5^{-1}n_5 + b_{43}\tau_4^{-1}n_4 - \tau_3^{-1}n_3 + x_a n_4 n_1 - \upsilon_a n_3 n_2 + 2x_b n_4 n_2 - 2\upsilon_b n_3^2 + x_c n_4 n_1 - \upsilon_c n_3 n_2 - x_d n_3 n_1 + \upsilon_d n_2^2, \quad (3)$$

$$\dot{n}_4 = b_{64}\tau_6^{-1}n_6 + b_{54}\tau_5^{-1}n_5 - \tau_4^{-1}n_4 - x_a n_4 n_1 + \upsilon_a n_3 n_2 - x_b n_4 n_2 + \upsilon_b n_3^2 - x_c n_4 n_1 + \upsilon_c n_3 n_2, \quad (4)$$

$$\dot{n}_5 = b_{65}\tau_6 n_6 - \tau_5^{-1}n_5, \quad (5)$$

$$\dot{n}_6 = R_{26} n_2 - \tau_6^{-1} n_6 . \quad (6)$$

The lifetime of the ith excited level for the isolated ion is given by τ_i. The branching ratio b_{ij} represents the percentage of the population in level i which decays by radiative relaxation to level j. The lifetimes and branching ratios were calculated using the Judd-Ofelt theory[14,15] and the intensity parameters given in Ref. 16.

The cross relaxation and upconversion energy transfer rates are described by the parameters x and υ, respectively. For the $(^3H_6, ^3H_4) \rightarrow (^3H_5, ^3H_5)$ cross relaxation process, a rate of 5.0×10^4 s^{-1} is given in Ref. 17. We emphasize that the values for each of the cross relaxation and upconversion rates differ since the values of the oscillator strengths vary depending on the initial level involved in the process. But, using the rate given for the cross relaxation process mentioned above, we have been able to determine the rates for all other interionic energy transfer processes by scaling in the following manner. Letting W_i represent any one of the cross relaxation or upconversion energy transfer rates,

$$W_i = \frac{1}{\overline{E}_{(i)}^2} R f_D^{(i)} f_A^{(i)} . \quad (7)$$

$\overline{E}_{(i)}$ represents the average energy difference of the donor emission and the acceptor absorption; $f_D^{(i)}$ and $f_A^{(i)}$ represent the oscillator strength of the donor emission and acceptor absorption transitions, respectively. R is proportional to the overlap integral for the donor emission and the acceptor absorption transitions; it is calculated from

$$R = \frac{W_d \overline{E}_{(d)}^2}{f_D^{(d)} f_A^{(d)}} \quad (8)$$

using W_d as the rate given above for the $(^3H_6, ^3H_4) \rightarrow (^3H_5, ^3H_5)$ cross relaxation process. The average energy difference for this same cross relaxation process is given by $\overline{E}_{(d)}$, and $f^{(d)}$ is the associated oscillator strength for this same process.

The values calculated for the lifetimes, branching ratios, cross relaxation rates, and upconversion rates can be found in Table II. The thermal distribution between the lower two levels is given by the τ_{th}^{-1} terms. This value was determined by calculating the Boltzmann distribution between the two lower levels using

$$\tau_{th}^{-1} = \tau_2^{-1} \exp \frac{hcE_{21}}{k_B T}, \quad (9)$$

where E_{21} is the energy difference, and T is the temperature in Kelvin. Except for the excited state pumping term R_{26} all of the spectroscopic parameters were known and held fixed.

TABLE II. Shown are the values used in the model for the lifetimes, branching ratios, cross relaxation, and upconversion rates. All values were calculated using the Judd-Ofelt theory.

Lifetime	Branching ratio
$\tau_6 = 12.5$ μs	$b_{65} = 0.010$
	$b_{64} = 0.055$
	$b_{63} = 0.649$
	$b_{61} = 0.286$
$\tau_5 = 905.0$ μs	$b_{54} = 0.054$
	$b_{53} = 0.281$
	$b_{52} = 0.616$
	$b_{51} = 0.049$
$\tau_4 = 702.7$ μs	$b_{43} = 0.027$
	$b_{42} = 0.205$
	$b_{41} = 0.768$
$\tau_3 = 18.1$ ms	$b_{32} = 0.440$
	$b_{31} = 0.560$
$\tau_2 = 42.0$ ms	
Cross relaxation	Upconversion
$x_a = 16851$ s^{-1}	$\upsilon_a = 7424$ s^{-1}
$x_b = 91549$ s^{-1}	$\upsilon_b = 41712$ s^{-1}
$x_c = 106463$ s^{-1}	$\upsilon_c = 46903$ s^{-1}
$x_d = 50000$ s^{-1}	$\upsilon_d = 48347$ s^{-1}

IV. NUMERICAL RESULTS

Two types of numerical results were of interest to us. We wanted to compare the predictions of our model to both steady-state and time dependent measurements in $LaCl_3:Pr^{3+}$ at liquid nitrogen temperature and room temperature. The steady-state solutions to our system of coupled rate equations gave information on the input laser intensity dependence of the fluorescence emitted from the $^3P_0$ level. The time dependent solutions provided information about the shape and magnitude of the buildup time of the $^3P_0$ fluorescence near threshold.

We found that our six-level system of coupled rate equations was unable to quantitatively reproduce both sets of experimental results. Our model was only successful at quantitatively describing the power dependence of the steady-state fluorescence emitted from the $^3P_0$ level. It has been shown[11] that the rate equation model requires the inclusion of the Gaussian intensity profile of the input beam in order to reproduce quantitatively the experimental results. Its inclusion is particularly necessary for allowing meaningful comparisons between the time dependent solutions and the time dependent measurements of the fluorescence near threshold. Kueny, Case, and Eden[18] were the first to point out that the Gaussian intensity profile of the input beam is an essential experimental consideration, although they did not incorporate it in their rate equation model. However, a model which did not include the Gaussian intensity profile of the input beam was useful in that it permitted us to obtain an initial estimate of the ESA cross section using the formula

$$\sigma_{ESA} = \frac{hcR_{26}}{\lambda_P I}, \quad (10)$$

where λ_P is the input beam wavelength, and I is the intensity of the input beam. An estimate of the ESA cross section was necessary for including the Gaussian intensity profile of the input beam.

In order to take into account the propagation of the input Gaussian beam, the sample had to be divided into discrete radial and longitudinal elements. We let r_i and z_i be the radial and longitudinal coordinate within the crystal, respec-

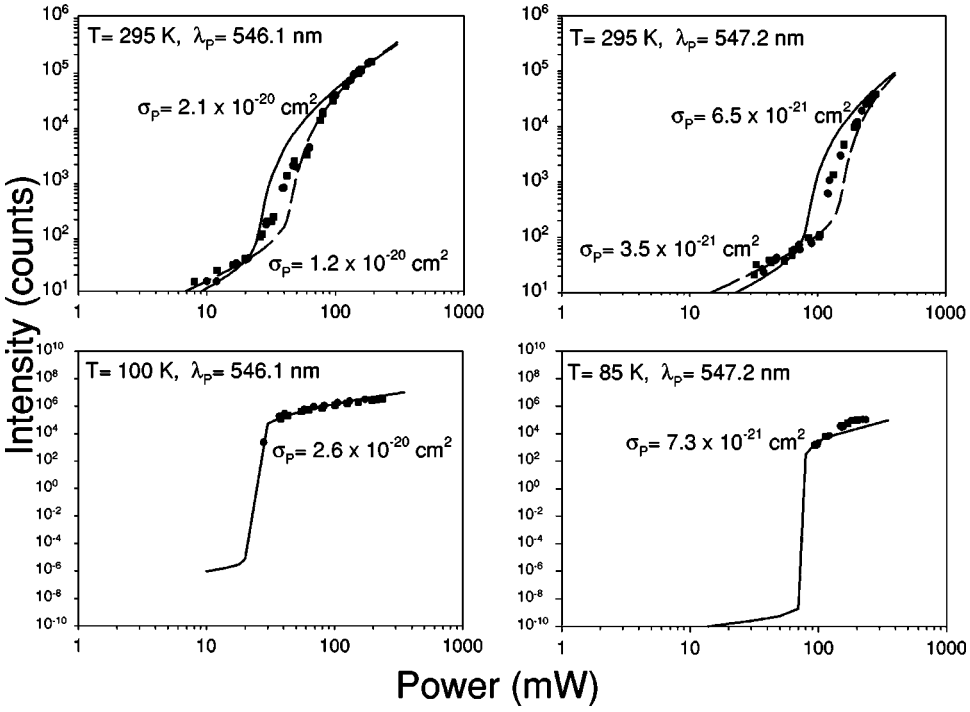

FIG. 2. Strength of the $^3P_0 \rightarrow {}^3F_2$ emission as a function of pump power at the focusing lens is shown for four different experimental situations. Circles and squares represent experimental data sets taken at different times. The lines are produced by a series of coupled rate equations combined with the propagation of a Gaussian input beam. Details of these calculations are given in Sec. IV.

tively. Since the input beam had a Rayleigh range of 9.2 mm, our crystal was thin enough ($\Delta l = 1$ mm) that only one longitudinal element $z_{i=1}$ was necessary to sufficiently describe the longitudinal propagation of the input beam. The radial elements were described by an inner and outer radii, $r_{in}(r_i)$ and $r_{out}(r_i)$, respectively. 100 radial elements, each with a width of 0.5 μm, were chosen for the calculation. The fraction of the power of the input Gaussian beam ρ_P contained in the cylinder located at the radial element r_i compared with the total pump power is given by

$$\rho_P(r_i) = \frac{2}{\pi w_P^2} \int_{r_{in}(r_i)}^{r_{out}(r_i)} \exp\left[\frac{-2r''^2}{w_P^2}\right] 2\pi r'' dr''$$

$$= \exp\left[\frac{-2r_{in}(r_i)^2}{w_P^2}\right] - \exp\left[\frac{-2r_{out}(r_i)^2}{w_P^2}\right], \quad (11)$$

where w_P is the radius of the beam waist. The pump rate per unit volume R_{26} is calculated using

$$R_{26}(r_i) = \{1 - \exp[-\Delta l(z_i)\alpha(r_i)]\}$$

$$\times \frac{\lambda_P}{hc} \frac{\eta_{in} P_{in} \rho_P(r_i)}{\Delta l(z_i)\pi[r_{out}(r_i)^2 - r_{in}(r_i)^2]}, \quad (12)$$

where P_{in} is the power incident on the focusing lens and η_{in} is the percentage of power transmitted into the crystal. The absorption coefficient is calculated from

$$\alpha(r_i) = \sigma_{ESA} n_2. \quad (13)$$

A Taylor expansion of the exponential term in Eq. (12) gives

$$R_{26}(r_i) = \alpha(r_i) \frac{\lambda_P}{hc} \frac{\eta_{in} P_{in} \rho_P(r_i)}{\pi[r_{out}(r_i)^2 - r_{in}(r_i)^2]}. \quad (14)$$

An adaptive step size fourth order Runge-Kutta integrator was used to obtain stable numerical solutions to our system of time dependent coupled rate equations. The only adjustable parameter included in the model was the ESA cross section σ_{ESA}. An initial estimate of this value was calculated for each transition at both room and liquid nitrogen temperatures using the rate equation model without including the input Gaussian beam intensity profile. Once the rate equations were combined with the propagation of the input Gaussian beam, the ESA cross section was adjusted to obtain the closest agreement between the numerical model and the experimental data.

The steady-state solutions to our system were determined by allowing the populations of the six levels to reach a constant value over a period of at least 4 s. Primarily, we investigated the power dependence of the upper level population n_6. This allowed us to make comparisons with our power dependent steady-state emission data in which we had focused our attention on the intensity of the fluorescence from $^3P_0 \rightarrow {}^3F_2$. Comparisons between the experiment and the model can be seen in Fig. 2. The strength of the $^3P_0 \rightarrow {}^3F_2$ emission as a function of P_{in} is indicated by the circles and squares in each of the four plots. We note that experimental data points are not shown below the critical threshold for either of the liquid nitrogen temperature data sets, since the emission is too weak to be observed below threshold. The model is represented by the lines drawn in Fig. 2. We note that both sets of room temperature data are described by two different ESA cross section values. We determined that one value of σ_{ESA} could not provide solutions which agreed with the experimental transients at all incident powers. The solid line represents the model which provides close agreement with the experimental transients taken at high powers, and the dashed line represents the model which provides close agreement with the experimental transients taken at lower powers.

The experimental transient data was compared to the pre-

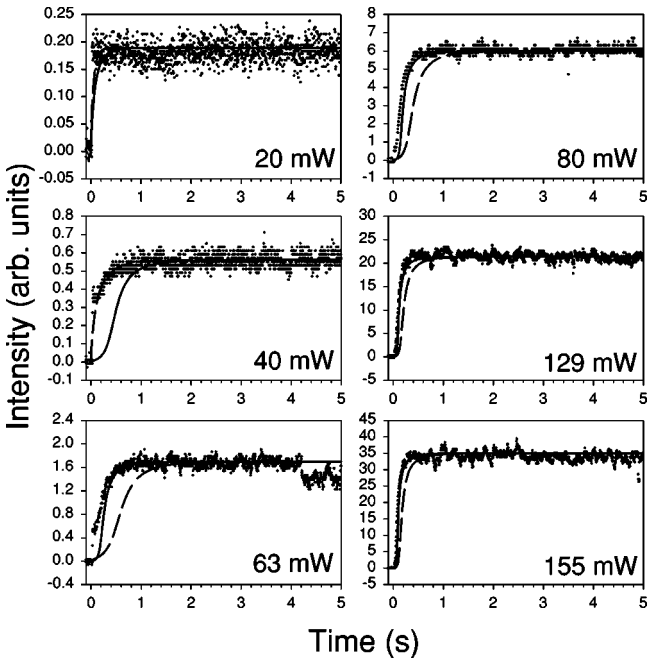

FIG. 3. Transients showing the buildup of the $^3P_0 \rightarrow {}^3F_2$ emission for six different laser powers, under 546.1 nm excitation at room temperature (295 K). The calculation of the solid and dashed lines is described in Sec. IV.

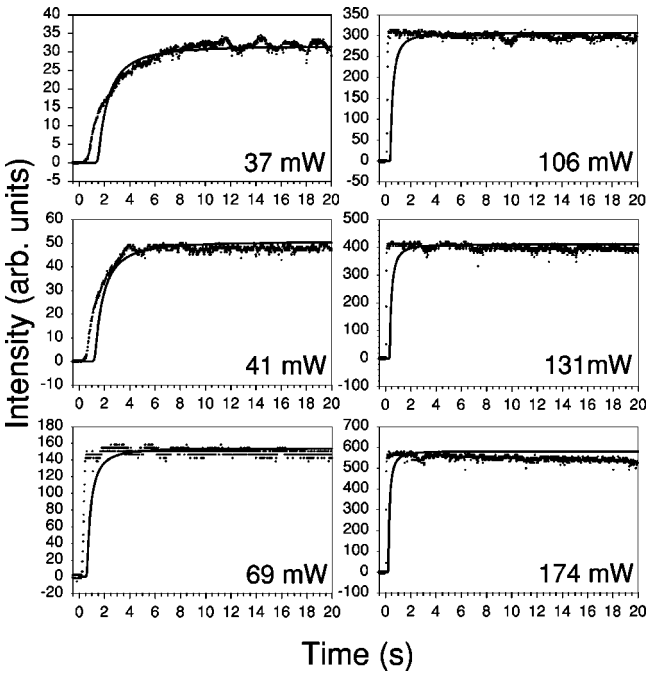

FIG. 4. Transients showing the buildup of the $^3P_0 \rightarrow {}^3F_2$ emission is shown for six different laser powers, under 546.1 nm excitation at liquid nitrogen temperature (100 K). The calculation of the solid line is described in Sec. IV.

dictions of our model for the time dependent behavior of the n_6 level population. These comparisons for the transition resulting from 546.1 nm excitation can be found in Fig. 3 for room temperature and Fig. 4 for liquid nitrogen temperature. In Figs. 3 and 4, we note that both the fluxations and decrease observed in the data once the system has reached steady state are due to small drifts in the power and frequency of the dye laser. In both Figs. 3 and 4 the ESA cross section values are the same as those presented in Fig. 2 for 546.1 nm excitation. Comparisons between the model and the experiment are not shown for the transition resulting from 547.2 nm excitation, however the results are similar to those shown for 546.1 nm excitation.

V. CONCLUSIONS

In this study, we tried to make a detailed treatment of the photon avalanche phenomenon in $LaCl_3:Pr^{3+}$ by constructing a model of the avalanche process and comparing this model to our experimental results. We generated two types of experimental data: (1) the laser power dependence of the steady-state fluorescence from $^3P_0$, and (2) the laser power dependence of the temporal behavior of the emission from $^3P_0$. Predictions from a model, consisting of a six-level system described by a series of coupled rate equations combined with the propagation of a Gaussian input beam, were compared with each of our experimental data types. We have shown that our rate equation analysis describes our system well at both room and liquid nitrogen temperatures. A comparison of experimental results with the predictions of our model enabled us to investigate systematically the impact of interionic processes on avalanche. Four cross relaxation processes and their associated upconversion processes were identified as being important. We have also determined that if the thermal population distribution between the lower levels of the system are included, it is unnecessary to include nonresonant GSA in our model as a starting mechanism for photon avalanche. Thus, we have been able to develop a model with only one adjustable parameter, the ESA cross section, which gives a good description of all of our experimental data. The model also allowed us to estimate values of the ESA cross section for the various $^3H_5 \rightarrow {}^3P_0$ pumping transitions at both room and liquid nitrogen temperatures. For the 546.1 nm transition at room temperature an average value of $(1.7 \pm 0.6) \times 10^{-20}$ cm^2 was determined for the ESA cross section. For the same transition at liquid nitrogen temperature a value of $(2.6 \pm 0.4) \times 10^{-20}$ cm^2 was calculated for the ESA cross section. For the 547.2 nm transition an average value of $(5.0 \pm 2.1) \times 10^{-21}$ cm^2 was determined at room temperature, and a value of $(7.3 \pm 0.8) \times 10^{-21}$ cm^2 was calculated at liquid nitrogen temperature for the ESA cross section.

ACKNOWLEDGMENTS

The authors wish to thank Dr. Joseph Ganem from Loyola College of Maryland for providing the crystal used in this work. We would also like to thank Dr. Hans Güdel and Dr. Markus Pollnau for helpful discussions.

[1] J.S. Chivian, W.E. Case, and D.D. Eden, Appl. Phys. Lett. **35**, 124 (1979).
[2] N. Bloembergen, Phys. Rev. Lett. **2**, 84 (1959).
[3] M.E. Koch, A.W. Kueny, and W.E. Case, Appl. Phys. Lett. **56**, 1083 (1990).
[4] W.E. Case, M.E. Koch, and A.W. Kueny, J. Lumin. **45**, 351 (1990).
[5] M.F. Joubert, Opt. Mater. **11**, 181 (1999).
[6] F. Pellé and P. Goldner, Acta Phys. Pol. A **90**, 197 (1996).
[7] W. Lenth and R.M. MacFarlane, J. Lumin. **45**, 346 (1990).
[8] M.F. Joubert, S. Guy, and B. Jacquier, Phys. Rev. B **48**, 10 031 (1993).
[9] F. Auzel and Y. Chen, J. Lumin. **65**, 45 (1995).
[10] B.C. Collings and A.J. Silversmith, J. Lumin. **62**, 271 (1994).
[11] S. Guy, M.F. Joubert, and B. Jacquier, Phys. Rev. B **55**, 8240 (1997).
[12] M. Wermuth and H.U. Güdel, J. Am. Chem. Soc. **121**, 10 102 (1999).
[13] S.M. Kirkpatrick, S.R. Bowman, and L.B. Shaw, J. Appl. Phys. **82**, 2759 (1997).
[14] B.R. Judd, Phys. Rev. **127**, 750 (1962).
[15] G.S. Ofelt, J. Chem. Phys. **37**, 511 (1962).
[16] L.B. Shaw, S.R. Bowman, B.J. Feldman, and J. Ganem, IEEE J. Quantum Electron. **32**, 2166 (1996).
[17] W.E. Case and J.S. Chivian, Bull. Am. Phys. Soc. **23**, 342 (1978).
[18] A.W. Kueny, W.E. Case, and M.E. Koch, J. Opt. Soc. Am. B **6**, 639 (1989).